Science Advances
AAAS

advances.sciencemag.org/cgi/content/full/5/5/eaav4028/DC1

Supplementary Materials for

Strain tolerance of two-dimensional crystal growth on curved surfaces

Kai Wang*, Alexander A. Puretzky, Zhili Hu, Bernadeta R. Srijanto, Xufan Li, Nitant Gupta, Henry Yu, Mengkun Tian, Masoud Mahjouri-Samani, Xiang Gao, Akinola Oyedele, Christopher M. Rouleau, Gyula Eres, Boris I. Yakobson, Mina Yoon, Kai Xiao*, David B. Geohegan*

*Corresponding author. Email: wangk@ornl.gov (K.W.); xiaok@ornl.gov (K.X.); geohegandb@ornl.gov (D.B.G.)

Published 31 May 2019, *Sci. Adv.* **5**, eaav4028 (2019)
DOI: 10.1126/sciadv.aav4028

This PDF file includes:

Section S1. Geometrical parameters of etched patterns and continuum elasticity analysis
Section S2. Additional structural, optical characterizations, and MD simulation for asymmetric strain distribution
Section S3. Detailed analysis for the simulations of multiple domain growth
Fig. S1. Geometrical parameters for photolithographically patterned trenches and donuts.
Fig. S2. Strain profile analysis for an ML MoS_2 crystal conforming to an individual donut as examined by a continuum elasticity model.
Fig. S3. Estimation of the intrinsic global strain in ML WS_2 crystals grown on SiO_2/Si substrates.
Fig. S4. Optical characterization of ML WS_2 crystals grown on 20-nm parallel trenches.
Fig. S5. Strain release and feature disappearance after detaching the ML from the 20-nm donut patterns.
Fig. S6. Description for the MD simulations and asymmetrical strain profile analysis by MD simulations by mimicking the growth process.
Fig. S7. Raman and SHG analysis for the crystals grown on 40-nm donuts.
Fig. S8. Morphologies of WS_2 flakes grown directly on 60- and 180-nm donuts.
Fig. S9. Phase-field simulation for multigrain-like shapes with different misorientation angles.
Fig. S10. First-principles density functional theory calculations.
Table S1. List of parameters used for the phase-field simulation.
References (*35*–*37*)

Section S1. Geometrical parameters of etched patterns and continuum elasticity analysis

1.1. Geometrical parameters for etched patterns of trenches and donuts

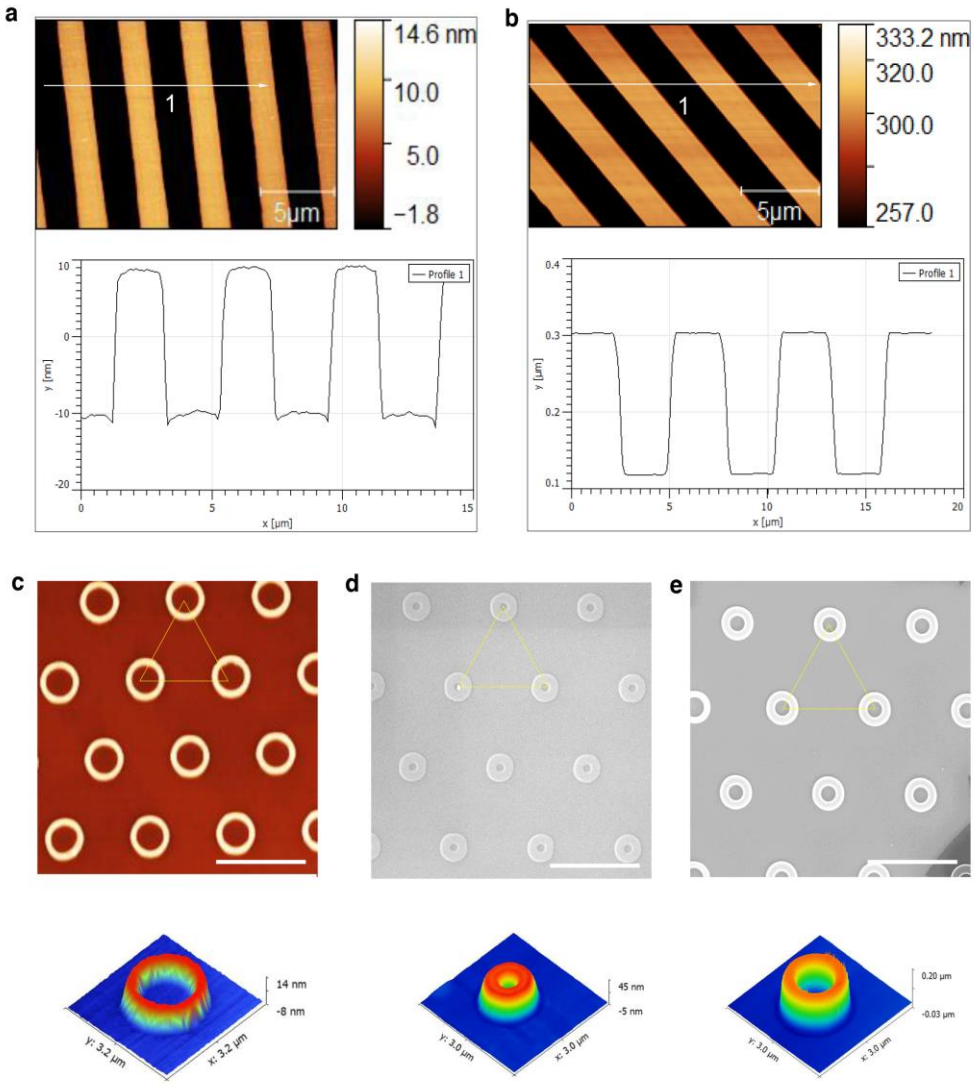

Fig. S1. Geometrical parameters for photolithographically patterned trenches and donuts. **a**,**b**, Upper: AFM images of trenches with a depth of 20 nm and 180 nm, respectively. Lower: Line profiles along white arrows in upper panels showing trench profiles. **c**-**e**, Upper: Representative AFM (**c**) and SEM images (**d**,**e**) of photolithographically patterned, hexagonally spaced (center-to-center spacing = 4 µm) donuts. Lower: Representative AFM 3D images for individual donuts with different heights. Note that the outer diameters of the donuts with heights of 20, 40, and 180 nm are 1.7, 1.3, and 1.6 µm, respectively.

1.2. Strain profile analysis in 2D crystals conforming to a donut by continuum elasticity model

A deeper insight into the strain redistribution by conformation to a curved geometry can be obtained through theory. The substrate creates mechanical strain in the material, and the strain further changes the band structure and band gap values. As described in the main text, the elastic response of WS_2 is isotropic; therefore, for a surface profile described as (x, y, $z(x,y)$), the induced stress/strain in the material is related to the surface profile *via* the second Föppl–von Kármán equation $(1/Y)\Delta^2\chi(x,y) + \left(z_{xx}z_{yy} - z_{xy}^2\right) = 0$; where Y is the Young's modulus and χ is the Airy stress function. Using deformation potential theory combined with symmetry arguments we show that the strain induced bandgap change for WS_2 is isotropic, with the relation

$$\Delta E_g^{WS_2} = D(u_{xx} + u_{yy}) = D\frac{1-\nu}{Y}(\chi_{xx} + \chi_{yy})$$

where D, u, and ν are the deformation potential, strain tensor, and Poisson ratio, respectively[35]. The coefficients Y, D, and ν can be obtained from experiments or *via ab initio* calculations, hence the bandgap change due to the substrate profile can, in principle, be completely determined. We have applied this analysis by solving the above equation numerically for experimentally obtained substrate geometries (AFM line profiles were extracted from fig. S1). The upper panels in fig. S2a-c show the AFM line profiles of donuts (gray) with different heights, which are fitted with error functions (black). The corresponding biaxial strains are shown in the bottom panels in fig. S2a-c. Corresponding band gap shifts induced by these strain levels for crystals conforming to 20-nm and 40-nm donuts are also shown in fig. S2d. The results for the 20-nm donut are -18 meV for the center, -7 meV for the body, and 0 meV outside the donut. For a crystal conforming to a 40-nm donut, the central region shows a variation in the

band gap from -50 meV to -230 meV. We also calculated the strain distribution for a 180-nm donut and found 17 % at the center, 5 % on the body, and 0% outside the donut. Clearly, the strain at the center is much higher than the breaking strain for WS_2 (~7% for MoS_2)[14], thus breaking or grain boundary formation is expected.

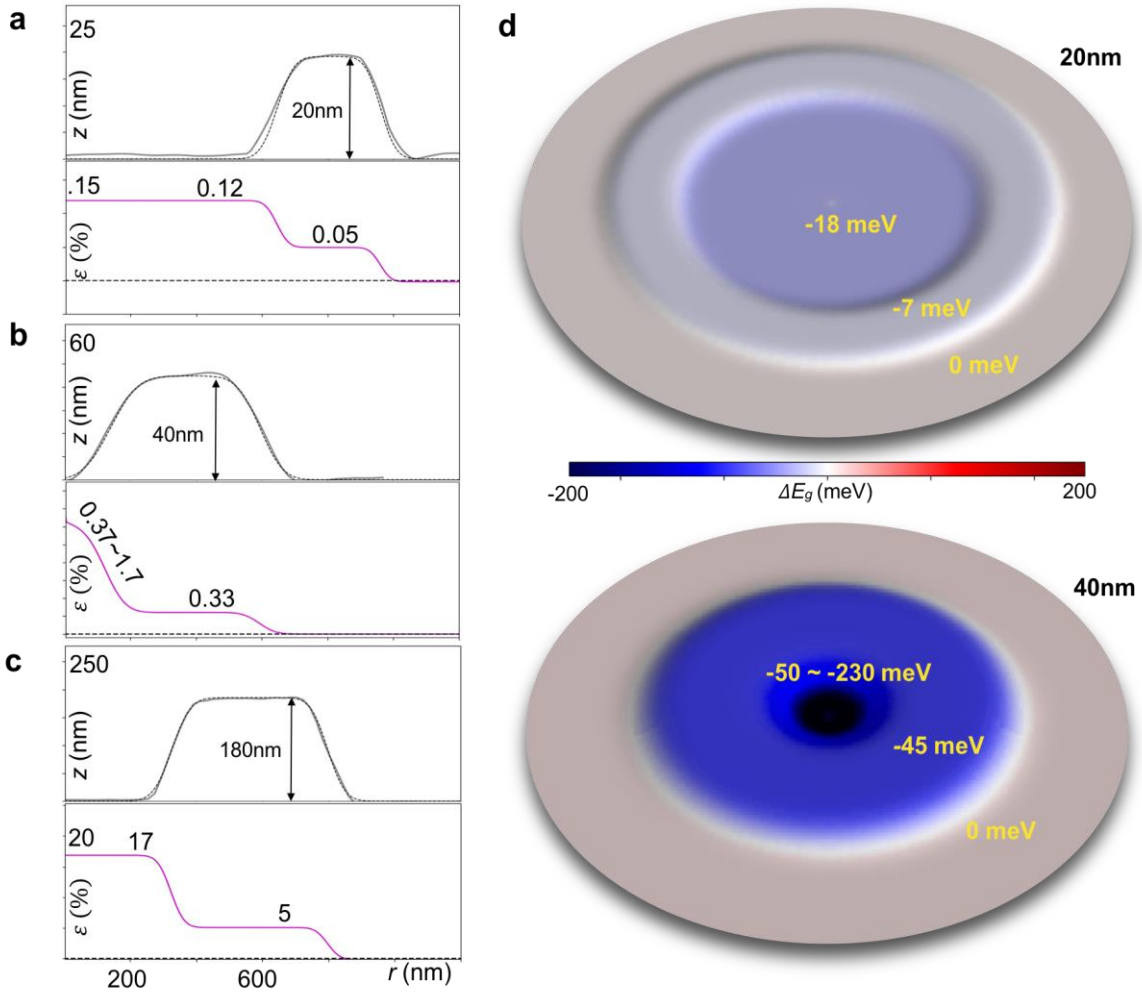

Fig. S2. Strain profile analysis for an ML MoS_2 crystal conforming to an individual donut as examined by a continuum elasticity model. a-c, upper panel: AFM radial height profile of the donut (gray), fit with error functions (black); bottom panel: radial profiles of the dilatational strain for the 20 nm, 40 nm and 180 nm donuts, respectively. **d**, Calculated band gap shift due to the biaxial strain for ML MoS_2 on a 20 nm (upper) and 40 nm (bottom) donut geometry, respectively. The analysis indicates that, before the crystal fractures, the strain distribution of the crystal on the donut is symmetric and the crystal region conforming to the center of donut has the maximum tensile strain. A high tensile strain of ~17% was calculated when the crystal conforms to the center of a 180 nm donut, implying that the crystal should fracture to release the strain.

Section S2. Additional structural, optical characterizations, and MD simulation for asymmetric strain distribution

2.1. Intrinsic global biaxial strain in as-grown WS_2 monolayers on SiO_2/Si substrates

As described in the Methods section, the WS_2 crystals were synthesized at 800 ^oC and collected after the CVD system cooled naturally down to room temperature. During the cool-down process, intrinsic global tensile strain builds up within the crystals because of the mismatch between the thermal coefficients of expansion of the WS_2 crystals and the growth substrate. To determine the intrinsic global strain in as-grown ML WS_2 on the SiO_2/Si substrate, we compared the room-temperature PL spectra was acquired on CVD-grown WS_2 MLs on SiO_2/Si substrates and *c*-cut sapphire substrates, suspended CVD-grown WS_2 MLs on TEM grids, and the WS_2 MLs transferred from the growth substrate (SiO_2/Si) to another SiO_2/Si substrate. We found that crystals grown on SiO_2/Si substrates were more strained than those directly grown on sapphire substrates. The suspended crystal on the TEM grid and the as-transferred crystals on SiO_2/Si substrate showed a neutral excitonic PL peak around 2.03 eV, indicating that the global tensile strain was released after transfer from the growth substrates. The previous theoretical calculation predicted a bandgap modulation of 135 meV per percentage of biaxial tensile strain for ML WS_2[20]. Therefore, we estimate the intrinsic global biaxial strain in as-grown WS_2 ML on SiO_2/Si in our system is ~0.4%. We also note that the intrinsic global strain had been previously estimated to be 1% within CVD-grown ML MoS_2 [26].

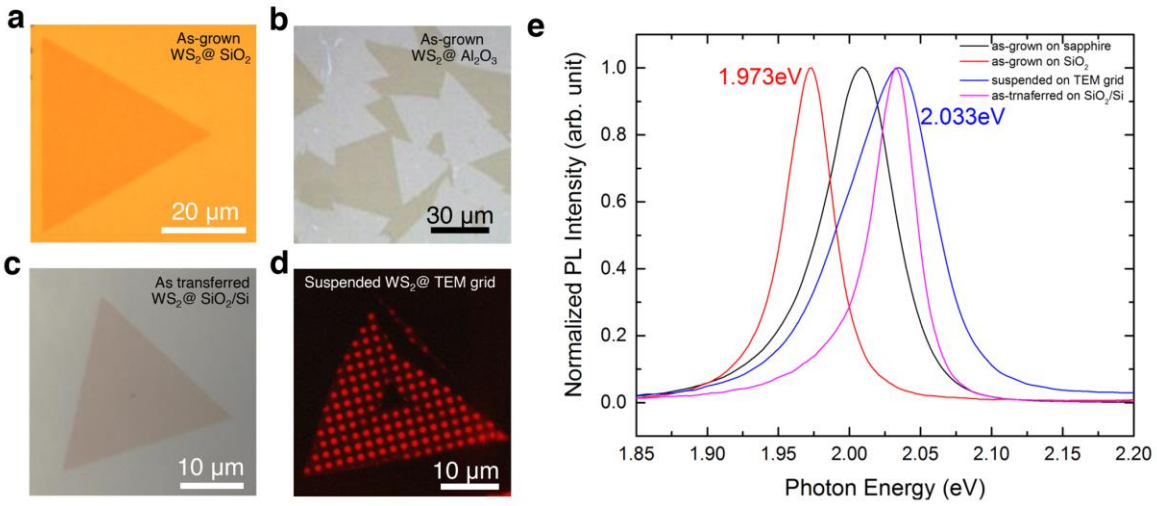

Fig. S3. Estimation of the intrinsic global strain in ML WS_2 crystals grown on SiO_2/Si substrates. a,**b**, Optical images of WS_2 crystals grown directly on SiO_2/Si and *c*-cut sapphire (Al_2O_3) substrates. **c**, Optical images of a CVD-grown WS_2 crystal after being transferred from the growth substrate to a flat SiO_2/Si substrate without annealing. **d**, Fluorescence (FL) image of an individual triangular WS_2 crystal on a TEM grid, where the WS_2 section with strong FL (bright) was considered to be substrate-free. **e**, Normalized PL spectra of WS_2 ML crystals excited with a 532-nm laser reveal that both the suspended ML WS_2 and as-transferred WS_2 crystals on SiO_2/Si appear to be almost strain-free, while an intrinsic global tensile strain of ~0.4% was determined for our CVD-grown WS_2 on SiO_2/Si substrates.

2.2. Morphologies and strain distribution for ML WS_2 grown on parallel trenches

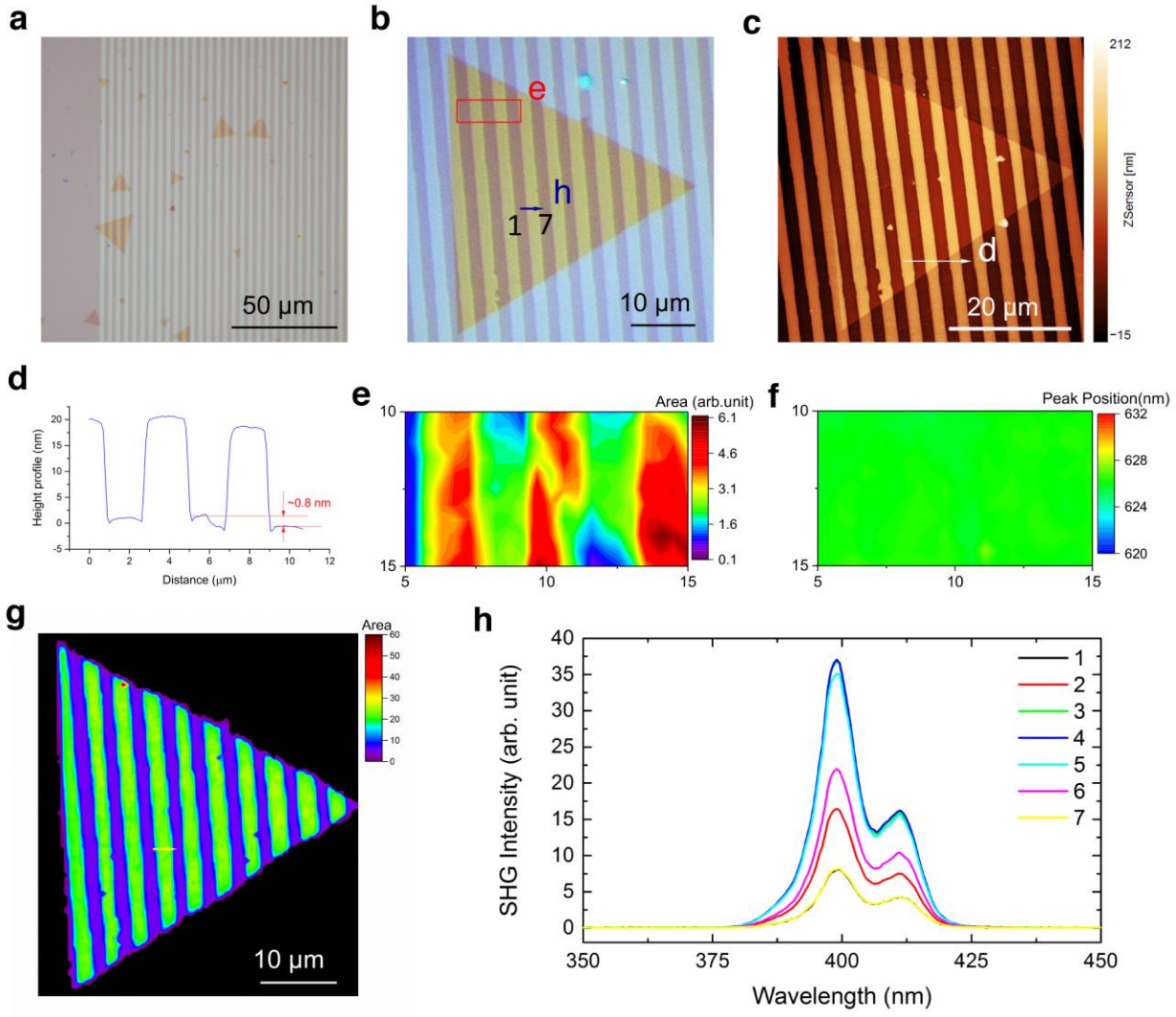

Fig. S4. Optical characterization of ML WS_2 crystals grown on 20-nm parallel trenches. a,**b**, Low and high magnification optical images of WS_2 crystals conforming to the 20-nm trenches. **c,** AFM image of an individual crystal shown in **b**. **d**, AFM height profile taken along a line labeled in **c**. **e**,**f**, spatial maps of PL intensity and peak position taken from the section of the crystal that was marked in the red box in **a**, indicating that no obvious strain variations was observed across the flake. The excitation laser has a wavelength of 532 nm and the PL intensity is integrated from 575 nm (2.16 eV) to 675 nm (1.84 eV) to produce the map. **g**, Spatial map of second harmonic generation (SHG) intensity for the ML WS_2 crystal in **b**, where the intensity was integrated from 370 nm to 420 nm. **h**, SHG spectra acquired from the line shown in **b** (scans 1 through 7).

2.3. Additional morphologies, optical spectroscopy, STEM, and detachment experiments on ML WS_2 grown on 20 nm donut patterns

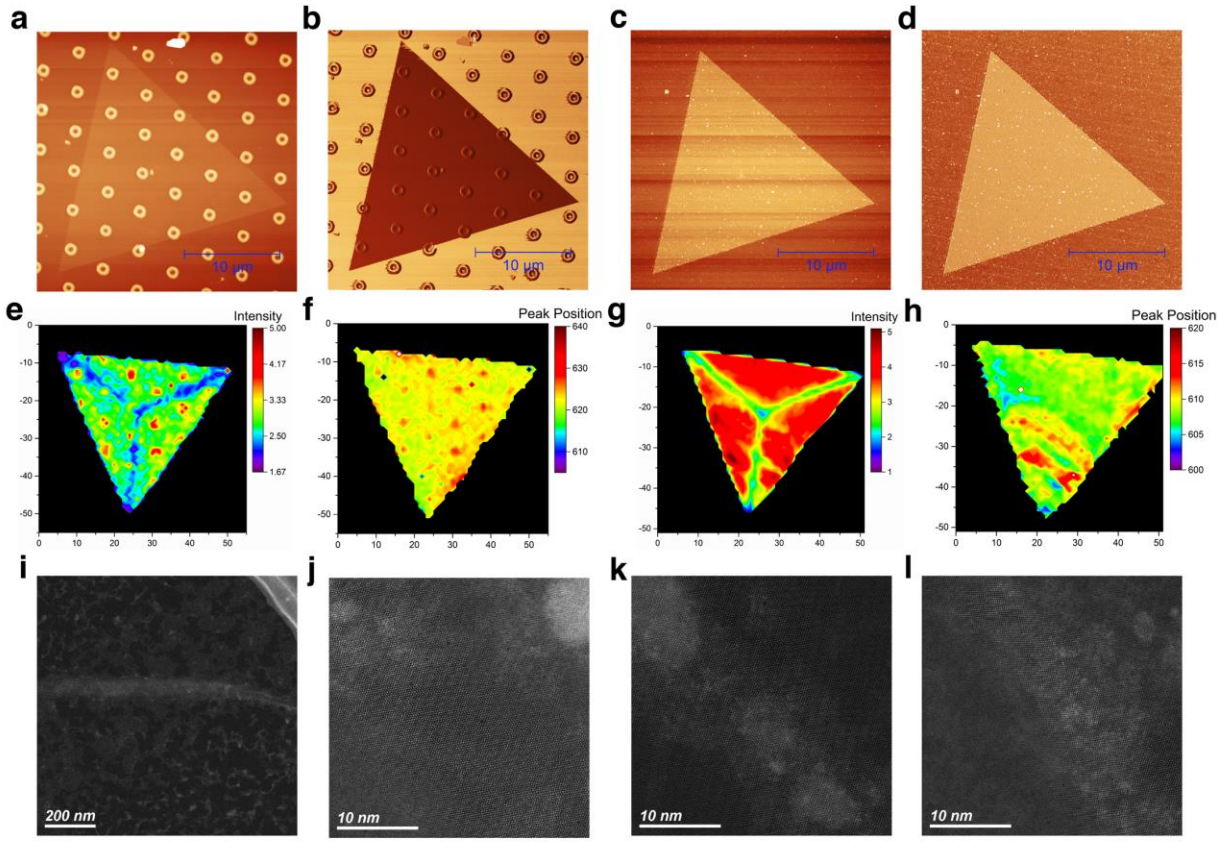

Fig. S5. Strain release and feature disappearance after detaching the ML from the 20-nm donut patterns. **a**, AFM height profile and **b**, phase image of a triangular WS_2 crystal grown directly on the 20 nm donut features. c, AFM height profile and **d**, phase image of the same flake transferred from the patterned substrate to a flat SiO_2/Si substrate. **e**,**f**, and **g**,**h**, Spatial maps of PL intensity ($\lambda_{Exc.} = 532\ nm$, integrated from 1.85 eV to 2.18 eV) and peak position (X^0) of the crystal before peeling off and after stamping onto the flat substrate. The variation in PL intensity and peak position that arise from the donut feature disappear after detaching the crystal from the donut pattern, further confirming the strain tolerant growth of 2D WS_2. **i**, low magnification of STEM images randomly taken from the ML crystal on the TEM grid. **j**-**l**, High magnification STEM images taken from different regions in **i**. All three images nearly show the same orientation of the crystal despite the wrinkles formed during the transfer process. In the specific areas of this flake, no freestanding donut-shaped features of WS_2 were discernible, which indicates that the stretched crystals that conformed to the donuts had no observable residual deformation after the strain was released.

2.4. Molecular dynamics simulation of asymmetric strain distribution in 2D crystal conforming to a donut

Our continuum elasticity model estimated the magnitude of the strain and the calculated strain distribution that generally matched with the experimental data, i.e., the maximum tensile strain was achieved in the center of the donuts (both for 2D crystals conform on 20-nm and 40-nm donut). However, an asymmetrical strain distribution was observed for the 2D crystal growth on 40-nm features that was clearly related to the growth direction of the 2D crystals. To investigate the asymmetry in the strain distribution, we simulated the growth process using molecular dynamics. We note that the actual growth process can be quite complicated to simulate as it involves several assumptions regarding the diffusion of adatoms, step nucleation, and other factors governing growth kinetics. Thus, we used a simplified model which mimics the growth process observed in the experiment, which progressed the edge one step at a time by adding an entire row of atoms, and then relaxing them on the substrate with the donut geometry. The important factors that cause the asymmetry are (1) the friction between the flake and the substrate, and (2) the size of the flake with respect to the lateral dimensions of the donut (its radius). Both factors limit the mobility of the atoms on the substrate, therefore restricting strain redistribution throughout the flake. In our simulations, due to computational limitations, we modeled large flakes by imposing a constraint on the non-growing edges in the direction perpendicular to the growth direction.

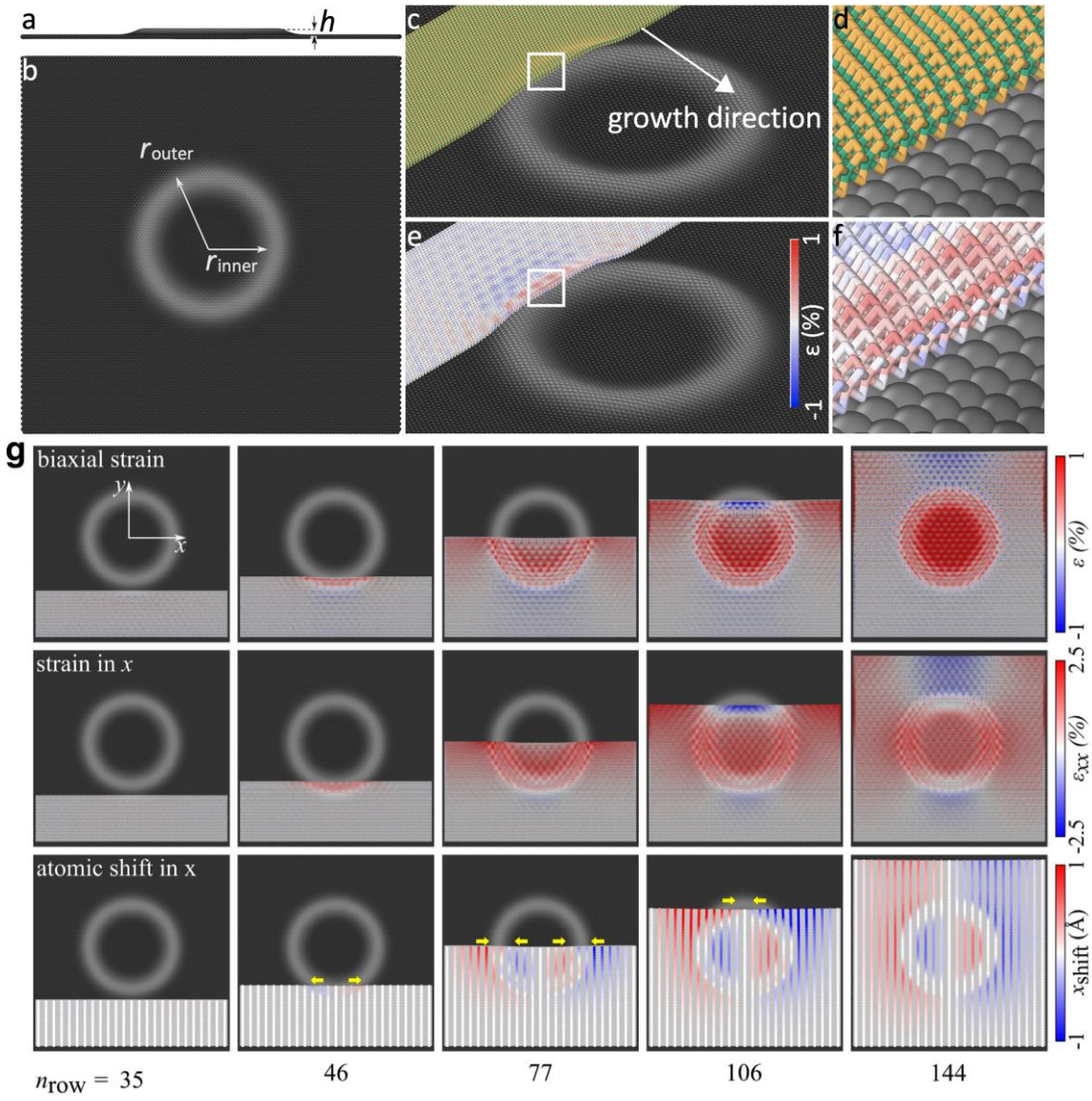

Fig. S6. Description for the MD simulations and asymmetrical strain profile analysis by MD simulations by mimicking the growth process. a and **b**, Substrate (side and top view, respectively) modeled as particles in a triangular lattice conformed to a donut geometry, with $h \approx$ 8 Å, $r_{inner} \approx 70$ Å and $r_{outer} \approx 100$ Å. **c**, MoS_2 flake on the substrate, yellow atoms are S and green are Mo. **e**, Atoms of (c) color-coded by the level of the biaxial strain ε. **d**,**f**, are the zoomed in views of the white framed region in (c, e), respectively. **g**, Snapshots from the MD simulation of the growth of a MoS_2 flake over a donut-shaped substrate, color-coded by the level of the biaxial strain (top row), strain in x (middle row) and atomic shift (in Å) of certain atoms in x (bottom row). Each column represents different stages of growth and is characterized by n_{row} which is the number of atomic rows added.

Note that the substrate in our simulations is modeled as a planar triangular lattice of particles that are displaced in the z-direction. It conforms to a donut geometry as shown in fig. S6 a and b. The substrate is modelled by a single layer of particles in a trigonal lattice (lattice constant $\approx$ 4 Å, chosen for convenience, and to keep the total number of particles, representing the substrate, low for computational efficiency.). The LJ potential is applied between these substrate particles and the Mo atoms in the MoS_2 ML. The adhesion energy (per unit area) between these layers, when they are completely flat can be derived to have the expression

$$\gamma_{adh} = 8\pi\rho_{sub}\rho_{mono}\epsilon\left[\frac{\sigma^{12}}{110\ d^{10}} - \frac{\sigma^{6}}{20\ d^{4}}\right]$$

Here, ρ_{sub} is the number density (number per area) of substrate particles, ρ_{mono} is the number density of the 2D material (MoS_2 units, lattice constant $\approx$ 3.16 Å), and d is the distance between the two layers (substrate and Mo-layer). One can further derive the equilibrium distance between the two layers as, $d_{eq} = \left(\frac{5}{11}\right)^{\frac{1}{6}}\sigma$.

Using these relations, we obtain

$$\gamma_{adh} = -\frac{6\pi}{125}\sqrt[3]{605}\,\rho_{sub}\rho_{mono}\epsilon\,\sigma^2$$

Plugging in the values, we obtain

$$\gamma_{adh} = -0.0266\ eV/\text{Å}^2$$

$$d_{eq} = 4.3843\ \text{Å}$$

The LJ parameters were chosen to resemble experimentally reported values for the adhesion energy of 2D materials to SiO_2 substrates.

To calculate the in-plane strain the MoS_2 flake was first transformed into a honeycomb lattice by averaging the positions of the S atoms (yellow) onto the Mo (green) atomic plane (fig. S6 c and d. The strain was then calculated by measuring the displacement of each atom with respect to a flake that was grown on a flat substrate. The color-coded atoms in fig. S6e and f show the biaxial strain for this configuration of atoms.

In fig. S6g, a MoS_2 flake at different stages of growth is shown, characterized by the number of rows added (n_{row}) and relaxed on the substrate. The asymmetry in the strain distribution is clearly observed in these simulations, and by their careful observation, we can propose an explanation for its origin. We note that a growing edge is a free boundary, and thus has zero normal stresses, which indicates that stresses on a growing edge should be uniaxial and along the edge length (x-direction). We, therefore, show the strain component in the x-direction in fig. S6g and use it to further explain the strain distribution. The strain in the y-direction is not plotted but is primarily just the result of the Poisson effect.

Initially, when the edge grows on the flat surface, the stresses in either direction remain essentially zero (until n_{row}=35) and the material does not accumulate strain. As the edge approaches the donut, it gets displaced out-of-plane (z-direction), which leads to its stretching as seen in the snapshot corresponding to ε_{xx} for n_{row}=46. When the edge has covered half of the donut (n_{row}=77), it is strained the most at the diameter of the donut, since the out-of-plane

displacement is maximum at the diameter. After this, the out-of-plane displacement decreases, but contrary to expectation, the strain distribution along the edge does not undergo a uniform decrease in magnitude. Instead, we see that the portion of the edge inside the donut becomes compressed, while the portions which are outside the donut become more stretched (n_{row}=106). This trend continues even as the edge continues growing outside the donut, and completely covers it at n_{row}=144.

To explain the latter behavior of the strain distribution we direct our attention to the bottom panel of fig. S6g. In this panel, we mark the changes in the x-position (or x_{shift}) of a few columns of atoms from an ideal straight line which should be their expected growth trajectory on a flat surface. A positive x_{shift} is marked red, and a negative x_{shift} blue. In the first two cases (n_{row}=35, 46), the vertical lines are almost completely white in color (except as it enters the donut), indicating no major x_{shift}, which is consistent with a negligible strain in these cases. When the donut is halfway covered, all edge atoms experience x_{shift} towards the periphery of the donut (as seen from yellow arrows). Therefore, we see a segregation of the edge into three segments, two outside and one inside the donut. The segments outside the donut continue to experience x_{shift} towards the periphery of the donut and, as a result, the outside segments keep stretching. The inside segment, however, experiences a decrease in the magnitude of the x_{shift} as it shrinks in size to zero, and the shifts from the outer segments create compressive strain in the central region (see yellow arrows). The continuation of these shift values outside the donut is thus observed and can be attributed to the friction between the substrate and the flake atoms. If there were no friction with the substrate, then this segregation of edge into three segments should not be expected, and we would see no asymmetry in the strain distribution before and after the donut.

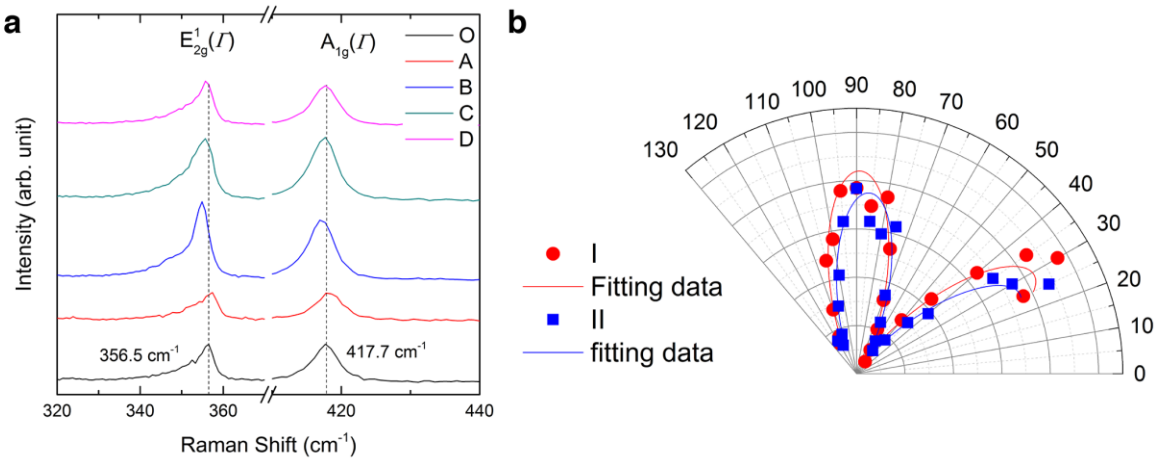

Fig. S7. Raman and SHG analysis for the crystals grown on 40-nm donuts. a, Raman spectra taken from the part of the WS_2 crystal that conforms to the center and edge of the donut, the neighboring flat substrate, and the neighboring strained area. Spectrum O is taken from WS_2 crystal grown on a flat substrate with the same crystal far from the donut. The selected locations corresponded to those in Fig. 4j. **b,** SHG data fitting used to determine the misorientation between areas I and II labeled in Fig. 4c in the main text.

The strain distribution in WS_2 grown on the 40-nm donuts can also be confirmed by Raman spectroscopy. For example, the in-plane and out-of-plane modes in the part of the crystal that conformed to the edge of the donut, spot B, softened by 1.6 cm^{-1} and 0.8 cm^{-1}, respectively, compared to the spectra obtained from the unstrained part (Fig. 4 j). Similar in-plane mode softening was found in the part of the crystal that conformed to the center of the donut and the most strained part, while the out-of-plane mode appears to be less sensitive to the biaxial tensile strain.

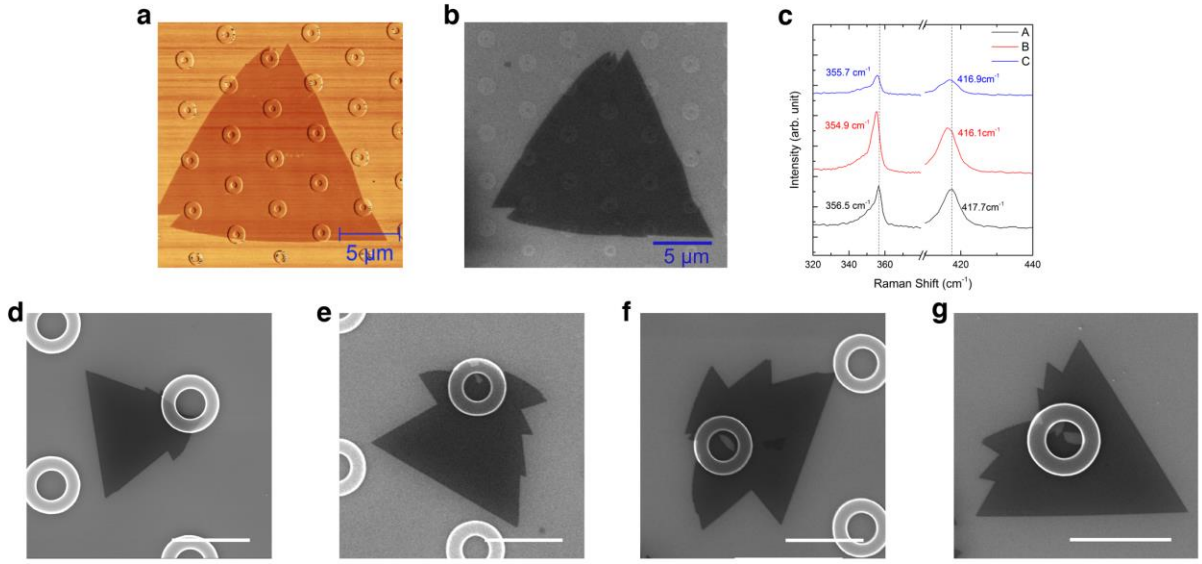

Fig. S8. Morphologies of WS_2 flakes grown directly on 60- and 180-nm donuts. **a-b**, a representative AFM image of ML WS_2 grown on a 60-nm donut showing the branched features, with corresponding SEM image in (b). **c**, Typical Raman spectra taken from the part of the WS_2 crystal in Fig. 5 that conforms to the center (C) and body of the donut (B), and the neighboring flat substrate along the growth direction (A). **d-g**, SEM images of WS_2 crystals showing branched features resulting from instances where an apex of the growing crystal engages a 180-nm donut feature. All the scale bars are 2 μm.

Section S3. Detailed analysis for the simulations of multiple domain growth

3.1 Phase-field simulation for a multi-grain-like shape

The misorientation at the GB on a flat substrate appears practically arbitrary. A phase-field simulation with the multi-phase-field model was undertaken to understand the resulting shapes. We consider only geometric rules. Despite the initial sprouted new orientation that occupies a tiny region, it generally has a prominent effect on the final shape. We use the phase-field model from Ref. 36. This model is for the growth of MoS_2 (a material that is like WS_2) and is based on the multi-component phase-field model[37]. A small modification is made – the supersaturation is kept at a constant value of 0.13 because we do not care about the growth instability. Also, if the grain grows onto the donut, then the growth speed will be slowed by 99%. We solve the model in *Matlab* through discretization with time steps of 0.01τ, and space-grid resolution of l. The boundary conditions are periodic, and a fast Fourier transform is used to get field variable derivatives. Other parameters are shown in Table S1.

Table S1. List of parameters used for the phase-field simulation. Tildes are omitted for dimensionless parameters.

Parameter	Symbol	Value
GB energy (C_6 term)	σ_1	1 eV/Å
GB energy (C_3 term)	σ_2	0.5 eV/Å
Characteristic length	l	50 nm
Interface thickness	η	$7l$
Coupling coefficient	λ	10
Mobility	μ_0	1

In the simulation, a canvas size of $300l \times 300l$ is set. The donut is modeled as a ring with an outer radius of $30l$ and an inner radius of $15l$ that is located at $(60l,0l)$. The grain starts from a circle with a radius of $10l$ at $(0l,0l)$. At a time of around 10τ, the grain meets the donut and has two contacting points along the right edge. Then, we place two new nuclei with radii of $5l$ that

sprout at the two contacting points. The two new nuclei are assigned the same new orientation and there is a misorientation between the sprouts and the main grain. Misorientations of 15˚, 30˚, 45˚, and 60˚ were examined, and the results are shown in fig. S9.

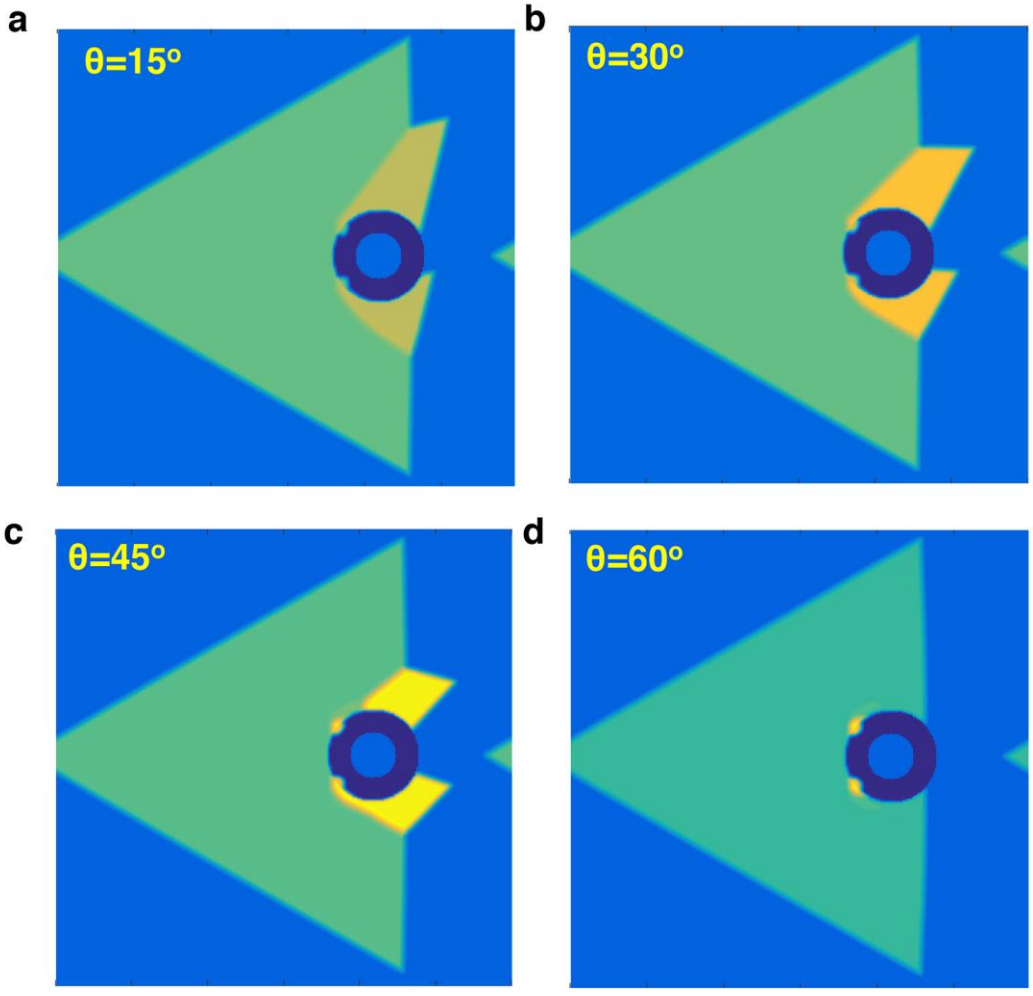

Fig. S9. Phase-field simulation for multigrain-like shapes with different misorientation angles. The misorientation between the main grain and the sprouts are 15˚, 30˚, 45˚, and 60˚ from a to d, respectively. Note that **a** contains an image that shows the growth trajectory.

3.2. First-principles density functional theory calculations for the energetics of creating edges

Here, we consider the energetics of creating edges that can serve as new growth nucleation sites. We employed first-principles density functional theory calculations to accurately capture their energetics. Specifically, we constructed 2D WS_2 nanoribbons terminated by either zigzag (ZZ) or armchair (AC) edge structures and investigated their energetics in terms of applied strains. It is an endothermic process to strain the film. For example, homogeneously straining a $1nm^2$ sheet by either 5% tensile strain costs ~2 eV, and the cost is almost doubled as the strain increases to 10% (fig. S10a). Therefore, a film located in a high strain environment, such as the highly curved substrate, needs to release this high strain energy by any means. One of the ways to release it is to be torn into parts, resulting in new edges. fig. S10b compares the energies of zigzag and armchair edges in terms of external strains either along the edges (σ_x) and perpendicular to the edges (σ_y), where the total energy per the length along the edge side is referenced to the edgeless perfect 2D sheet and all the structures are under the same types of strains. The edge energy is evaluated as $\frac{\Delta E}{L} = \left(E_{2D} - 2E_{L/2}\right)/L$, where $E_{2D}$is the energy of a 2D sheet that is equally split into two 2D flakes of energy $E_{L/2}$ with the length of edge L/2. Here we assume that the edge structures are under the same amount of strains as the parental structure. The edge energy also increases as the tensile strain is applied, where the increase is much higher with AC edge structure than with the ZZ edge structure. Our calculation shows that the energy cost with creating edges is higher than that of the edgeless structure, thus edges are unfavorable under a tensile strain. On the other hand, under a high compressive strain of <12% for ZZ and <17% for AC, the edge structures become energetically more stable than the structure without edges, therefore the creation of new edges serves as the way to release the strain energy.

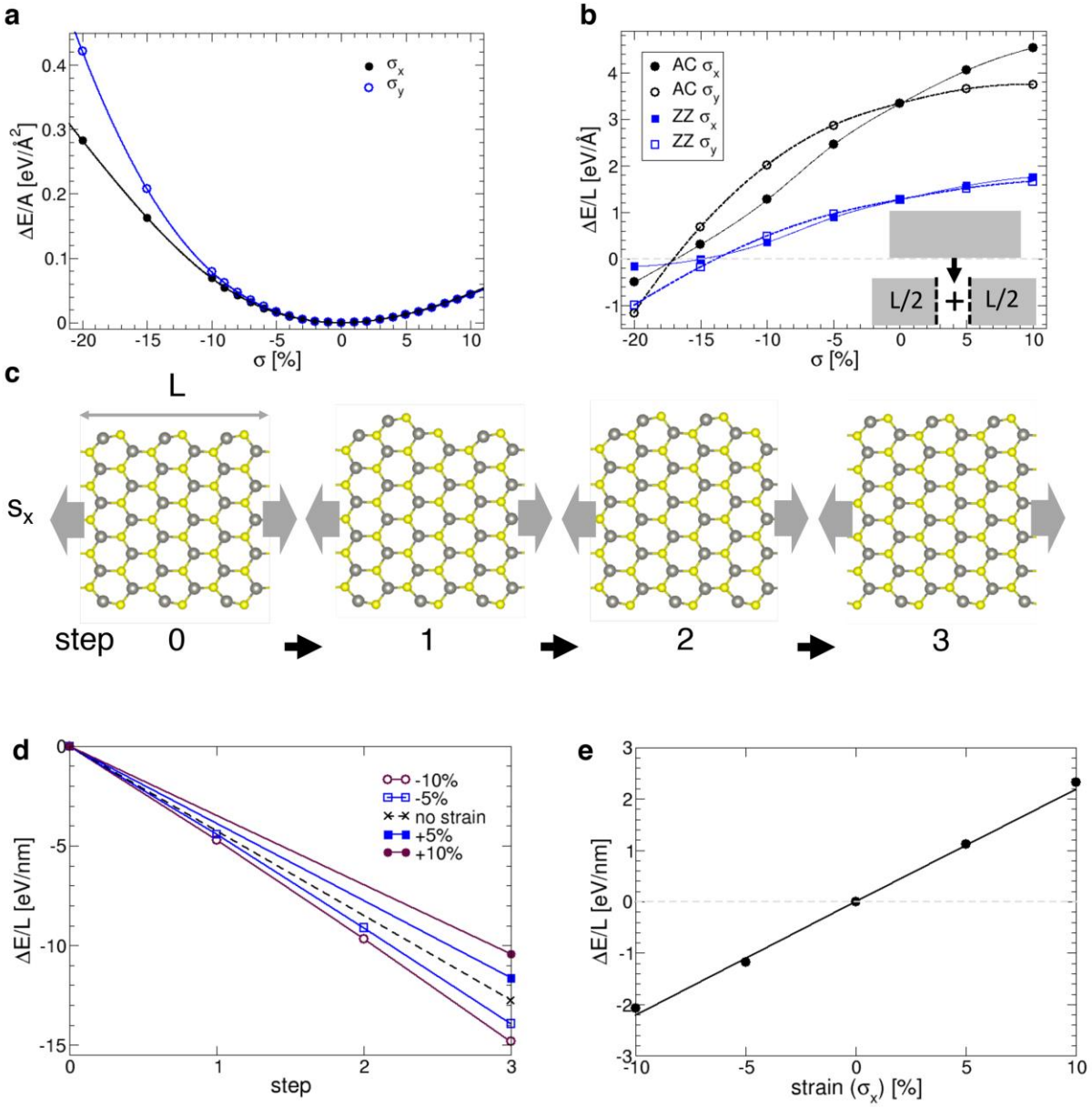

Fig. S10. First-principles density functional theory calculations. a, Energy cost to homogeneously strain a perfect, edgeless 2D WS_2 crystal, where the strain is applied either along the W-S bond direction in 2D space (σ_x) or perpendicular to the bond direction. **b,** Energies of 2D WS_2 edges in terms of external strains along the edges (σ_x) and perpendicular to the edges (σ_y), where zigzag (ZZ) and armchair (AC) edges were considered and the reference energy is an edgeless 2D sheet. **c-e** Atomistic modeling of strain effects on the growth process. **c**, Atomistic modeling testing the feasibility of edge growth formation where uniaxial strain (σ_x) is applied during the growth process. **d**, Changes in the energy per unit length as a function of the growth processes and applied tensile (+)/compressive (-) strain. **e**, the energy cost to complete the growth process by adding a layer, where the reference energy is the one without any strain.

Figure S10c illustrates a feasible growth process where the film grows by sequentially adding a WS_2 trimer. We investigate the energetics of the growth process that consists of the initial state (0) to the next step by adding a WS_2 trimer (1), and the step goes on until the addition of the one layer is completed. We monitor the changes in total energy during the growth process as a function of uniaxial strain along the armchair direction (see fig. S10a), either compressive or tensile strain as presented in fig. S10d. Overall the growth process is energetically favorable. Thus, the continuous growth process is always supported under strain. As the total energy is continuously lowered the total energy is defined as the energy with respect to the initial state (step 0) and the gaseous state of WS_2. However, the amount of energy gain during the growth process differs noticeably. A tensile strain of over 5% induces a significant reconstruction of the armchair edge structures, which makes the structure very unstable under tensile strain and results in a growth process less energetically favorable with respect to the no-strain condition. We calculated the energy gain by adding a layer from the gas phase of WS_2 and the initial state, per unit length, and compared it as a function of applied strain with that using the no-strain energy as a reference. Fig. S10e clearly supports the conclusion that the growth process becomes much more energetically favorable under compressive strain, but less favorable under tensile strain, where the energy gain/cost under the strain is $\sim\pm|\sigma_x|$ 0.22eV/nm, where energy gain is negative (-) for the compressive strain and energy cost is positive (+) for the tensile strain. Our first-principles atomistic calculation supports the experimental finding that the strain strongly affects the speed of the growth process.